International Journal of Microwave and Wireless Technologies, 2017, 10(2), 243–251.
doi:10.1017/S1759078717000526

RESEARCH PAPER

High-selective band-reject FSS with dual-band near-zero refractive index based on complementary dual-layer symmetry resonator-ring

RUI XI, LONG LI, YAN SHI, CHENG ZHU AND XI CHEN

A new band-reject frequency-selective surface (FSS) based on dual-band near-zero refractive index metamaterial (ZIM) design is presented in this paper. Consisting of a planar array of complementary dual-layer symmetry resonant ring, the proposed FSS exhibits a high-selective band-reject filtering response. From the viewpoint of effective medium, the subwavelength FSS is characterized by near-zero effective magnetic permeability and near-zero effective electric permittivity in two different operational bands, respectively. The corresponding resonant behavior and E-field distributions are analyzed in detail. A prototype of the proposed FSS working in X-band is fabricated and measured. The simulation and experiment results verify the effectiveness and correctness of the ZIM-based design method.

Keywords: Band-reject filtering response, Dual-band, Effective media, Frequency-selective surface (FSS), High selective, Near-zero refractive index metamaterial (ZIM)

Received 8 November 2016; Revised 7 April 2017; Accepted 10 April 2017; first published online 6 December 2017

I. INTRODUCTION

In recent years, frequency-selective surfaces (FSSs) have drawn extensive attention of many researches in spatial filters, antenna radomes for RCS (radar cross-section) controlling, and Cassegrain reflector antennas [1–3]. As spatial filters, FSS can be designed to exhibit band-pass and band-stop responses [1], respectively. A typical single layer FSS consists of two-dimensional (2D) periodic array of unit cells, and it is well known that its filtering response suffers from poor selectivity and narrow bandwidth. To improve its filtering characteristics, cascading multilayer FSS is a common technique [4, 5]. Other methods have also been reported lately, for example, a 3D FSS [6], SIW (substrate integrated waveguide) design [7, 8], and 2D periodic array of vertical microstrip lines [9, 10]. However, it is not easy to achieve good selectivity response with planar layered band-reject FSSs due to the lack of enough coupling.

Researches in near-zero refractive index metamaterials (ZIM) [11, 12] have attracted much attention over the past decades. Based on the effective media characteristics, ZIM can be classified into three categories: magnetic permeability (μ) is near-zero metamaterial (MNZ), electric permittivity (ε) is near-zero metamaterial (ENZ), and both permeability and permittivity are near-zero metamaterial (DNZ). It has been demonstrated that a ZIM is capable of reshaping phase and concentrating beams in a small zone [13, 14]. However, impedance mismatch will occur for ENZ and MNZ cases due to their wave impedance $\eta = \sqrt{\mu/\varepsilon}$ approaches infinity and zero, respectively. Good transmission can be achieved for DNZ case, of which impedance is equal to the impedance of free space, and thus the normalized impedance is $\eta = 1$. It is worth noting that nearly full transmission of electromagnetic energy is allowed for the ENZ case even in the presence of strong impedance mismatch [15]. This charming phenomenon is the inherent ability of the ENZ to squeeze and tunnel electromagnetic energy through narrow subwavelength waveguide channels [16]. These specific effective media properties can be effectively adopted to design a FSS for the band-reject or band-pass filtering characteristics.

In this paper, we propose a new design of band-reject FSS exhibiting dual-band near-zero refractive index with MNZ and ENZ properties. The element of complementary dual-layer symmetry resonator-ring (CDSRR) is designed to support magnetic and electric Lorentz models [17] in two different frequency bands, respectively. A good pseudo elliptic band-reject filtering response is thus realized by coupling the two resonant modes. Based on its effective medium characteristics extracted from the *S*-parameters [18], a new insight into the band-reject FSS's filtering responses has been given. It should be noted that not only the transmission zeros and poles can be adjusted, but also the ENZ tunneling frequency of the FSS can be independently controlled, which makes it convenient for specific filtering design. The proposed FSS based on

School of Electronic Engineering, Collaborative Innovation Center of Information Sensing and Understanding, Xidian University, Xi'an, China
Corresponding author:
L. Li
Email: lilong@mail.xidian.edu.cn

ZIM model has some advantages, such as high-selectivity, low-profile, easy fabrication, etc. It also has a potential application value in spatial filtering and antenna beam shaping.

This paper is organized as follows. Section II introduces the design and configuration of the proposed CDSRR FSS. The analytical model is presented based on the effective medium characteristics. Section III gives an optimized parametric study of the new structure based on the analytical model presented in Section II. Then, the fabrication and measurement of the FSS prototype working in X-band are presented in Section IV. Finally, a brief conclusion of this work is drawn in Section V.

II. CDSRR FSS DESIGN AND CONFIGURATION

The geometrical pattern of the proposed CDSRR FSS is shown in Fig. 1(a). The metallic pattern symmetrical about *y*- and *z*-axes is printed on both sides of the substrate with thickness $h = 3.0$ mm, relative permittivity $\varepsilon_r = 2.65$, and loss-tangent $\tan\delta_c = 0.0013$. The thickness h is approximately $\lambda/12$ (λ is the operational wavelength in free space), which is a low-profile design. It consists of a square patch etched by an annular slot, a pair of rectangular slots on both side arms along the *z*-axis with width $gap_2 = 3$ mm, and two pairs of orthogonal rectangular slots rotated $\pm 45^\circ$ from the *z*-axis with width $w_1 = 3$ mm and $w_2 = 4$ mm, respectively. The dimension of the square patch is $P = 18$ mm. The inner radius and outer radius of the annular slot are $a = 6.3$ mm and $b = 8.7$ mm, respectively. In addition, this pattern is surrounded by a square ring slot with width $gap_1 = 0.3$ mm. Figure 1(b) shows the simulation model of unit cell of the proposed CDSRR FSS in a TEM waveguide using Ansys HFSS. As is illustrated, the unit cell can be arranged and arrayed along *y*- and *z*-axes since the *E*-field is applied along the *y*-axis, while the *H*-field along the *z*-axis with a normal incidence along the *x*-axis. Based on the traditional theoretical guidance presented in [20, 21], in which an electrically coupled magnetic resonance is produced by a split-ring resonator (SRR) and an electric Lorentz model is formed by an electric inductive–capacitive resonator (ELC). Inspired by this phenomenon, we design the CDSRR pattern as the geometry of the unit cell to produce a dual-band near-zero refractive index performance. The systematic connection between the geometrical features of the CDSRR pattern and the expected electrical response can be described as follows.

Firstly, as can be observed from Fig. 1, the CDSRR pattern is designed as the complementary structure of a SRR with polarization configured in accordance with the dual sources in Babinet's principle [22]. The original SRR is obtained by replacing the metal parts of the CDSRR structure with apertures, and the apertures with metal plates. Then the SRR gaps are formed by the right- and left-side arms along the *y*-axis with width $gap_2 = 3$ mm. As has been demonstrated in [21], when the *E*-field is applied parallel to the gap-bearing side of the SRR with direction of propagation perpendicular to the SRR plane, a magnetic dipole can be obtained to achieve a negative permeability. However, it should be noted that the electrically coupled magnetic resonance is an indirect one, and it is inevitably weak compared with the magnetic resonance excited by the magnetic field directly normal to the SRR plane. On the other hand, the CDSRR pattern is designed as an ELC with the upper and lower side arms along the *z*-axis served as the electric resonant arms. Capacitor is formed between adjacent electric resonant arms arranged periodically along the *y*-axis, an electric Lorentz model can be possibly produced to achieve a negative permittivity. This expected electrical response can be confirmed in Fig. 2(d), in which the simulated effective permeability and permittivity both exhibit a negative value.

Secondly, transmission zeros also appear at f_3 and f_4 with strong magnetic and electric resonance as shown in Figs 2(a) and 2(d), and thus a stop-band is formed between f_3 and f_4. To form a stop-band spatial filter with good selectivity, we should separate the resonant frequencies of the negative permittivity and the negative permeability apart. The CDSRR pattern is etched by an annular slot and two pairs of orthogonal rectangular slots rotated $\pm 45^\circ$ from the *z*-axis, the capacitance to adjacent cells is dramatically enhanced and consequently, the resonant frequencies of the electric and magnetic Lorentz models are reduced to lower

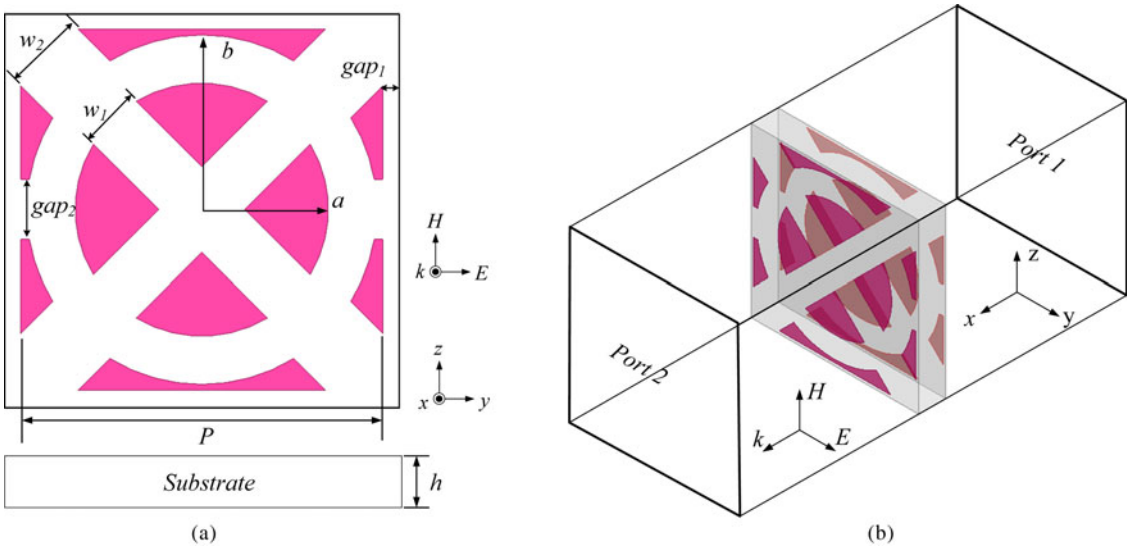

Fig. 1. Geometry of the proposed CDSRR FSS. (a) Top view of the unit cell, and (b) simulation configuration.

https://doi.org/10.1017/S1759078717000526 Published online by Cambridge University Press

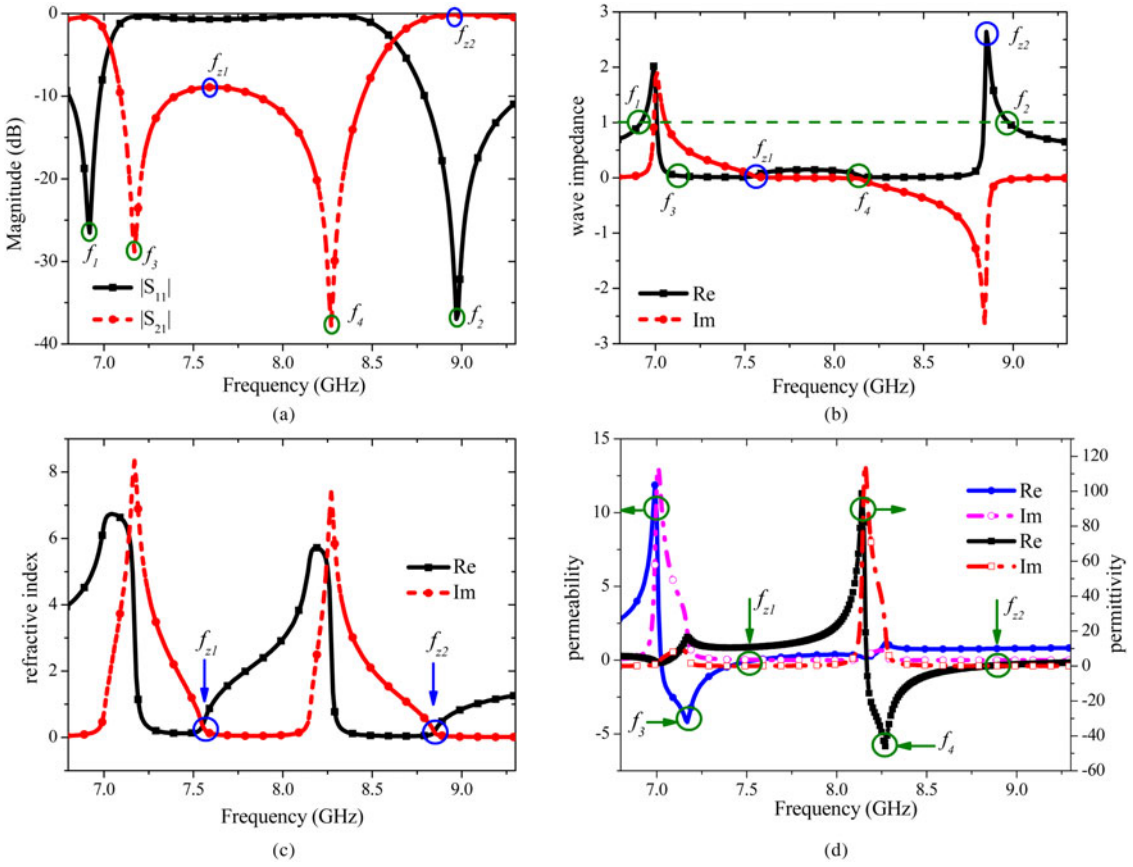

Fig. 2. Simulated *S* parameters and extracted effective constitutive parameters of the proposed CSDRR FSS unit cell. (a) Filtering responses, (b) normalized wave impedance, (c) effective index of refraction, and (d) effective permeability and permittivity.

frequencies. By carefully adjusting the dimensions of the slots, we can separate the resonant frequencies of the electric and magnetic resonances apart. Experimental results later shown in this paper can reasonably reproduce the simulation performance. As will be discussed in Section III, the simulated filtering response of the unit cell can be optimized by carefully adjusting w_1, w_2, and b of the slots and gaps. Therefore, the resonant frequencies of the negative permittivity and the negative permeability can also be affected due to the inner relations between them, as will be described in the subsequent part of Section II. As can be observed in Fig. 2(c), a dual-band near-zero refractive index performance is thus formed. This performance can also be demonstrated by experimental results later shown in this paper.

In addition, the transmission coefficient will arrive at the peaks for the near-zero refractive frequencies due to the concentrating beam property [13, 14]. Based on these special characteristics, we can then design the band-pass and band-reject performance of the ZIM, which makes the CDSRR as ZIM unit cell but also FSS cell. The CDSRR FSS can exhibit a high-selective band-reject filtering response with dual-band near-zero refractive index properties.

The simulated *S* parameters and normalized wave impedance of the proposed CSDRR FSS unit cell are shown in Figs 2(a) and 2(b), respectively. It can be seen from the reflection response that the bandwidth ratio of -3 to -0.5 dB is 1.18, and the reflection response around 8.78 GHz drops from -3 dB to the reflection zero of -38.8 dB in <350 MHz, thus resulting in a higher selectivity than a conventional FSS. Two reflection zeros of $f_1 = 6.91$ GHz, $f_2 = 8.95$ GHz and two reflection poles of $f_3 = 7.17$ GHz, $f_4 = 8.26$ GHz of the proposed CSDRR FSS are also observed in Fig. 2(a). The extracted refractive index, permeability and permittivity are shown in Figs 2(c) and 2(d), respectively. We can observe from Fig. 2(c) that the proposed FSS has two zero-refractive-index frequency points $f_{z1} = 7.55$ GHz and $f_{z2} = 8.83$ GHz produced by near-zero permeability and near-zero permittivity, respectively.

The extraction method for the effective medium parameters was presented in [18]. It is well known that in the interface between artificial material slab and free-space, *S* parameters scattering at normal incidence for a symmetrical material with thickness h can be given as

$$S_{11} = S_{22} = \frac{(\eta^2 - 1)(1 - Z^2)}{(\eta + 1)^2 - (\eta - 1)^2 Z^2}, \quad (1)$$

$$S_{12} = S_{21} = \frac{4\eta Z}{(\eta + 1)^2 - (\eta - 1)^2 Z^2}, \quad (2)$$

where η represents the normalized wave impedance of the material, $Z = \exp(-jkh)$ is the transmission term, k is the wave number in free space, μ_e and ε_e are the effective permeability and effective permittivity, respectively. The normalized wave impedance η is defined as $\eta = \sqrt{\mu_e/\varepsilon_e}$. As can be speculated from the permeability and permittivity shown in Fig. 2(d), the values of the normalized wave impedance can be calculated. In addition, it should be noticed that all the

https://doi.org/10.1017/S1759078717000526 Published online by Cambridge University Press

effective permittivity, effective permeability, and the normalized wave impedance are defined in the form of complex value, which include not only real part, but also imaginary part. The normalized wave impedance is presented in Fig. 2(b), in which η approaches zero and maximum at zero-refractive-index frequency points f_{z1} and f_{z2} can be explained in terms of the near-zero μ_e and near-zero ε_e, respectively. It can be further observed from Figs 2(a) and 2(b) that η is almost equal to one at two reflection zeros of f_1 and f_2, where the impedance are well matched. However, resonant frequencies f_3 and f_4 are defined as reflection poles, where the normalized wave impedance η is almost equal to zero. What's more, transmission zeros also appear at f_3 and f_4 with strong magnetic and electric resonance as shown in Fig. 2(d). Thus, a stop-band is formed between f_3 and f_4 due to the mismatched impedance, which can also be observed in Fig. 2(a). It should be noticed from Figs 2(b) and (2d) that the η resonances at f_3 and f_4 correspond to the negative resonance peak of μ_e and ε_e, respectively. Based on the analytical model above, it is clearly clarified that η builds not only a bridge between reflection resonant frequency points and zero-refractive-index frequency points, but also determines the filtering responses of the proposed FSS.

Additionally, an interesting property can be observed in Figs 2(a) and 2(b) that a good transmission is achieved at zero-refractive-index (ENZ) frequency point f_{z2} though η approaches maximum. This phenomenon is, in fact, a consequence of the ENZ tunneling effect due to the near-zero permittivity characteristic of the proposed FSS. With excitation assigned on Port 2 in Fig. 1(b), the electric field distributions in the *xoy*-plane at reflection resonances and zero-refractive-index frequencies are shown in Fig. 3. As expected, the electric field is concentrated on the FSS at the tunneling frequency f_{z2}. Good power transmissions are also clearly noted at f_1 and f_2, which demonstrate the fact that η is matched to the free space. On the contrary, for electric distributions at f_3, f_4, and f_{z1}, the power can barely transmit the structure, while most of the power is reflected.

Electric field distributions of the proposed FSS at reflection resonances and zero-refractive-index frequencies are illustrated in Fig. 4 to provide a reference and guideline for further analysis of the filtering response, red parts on the electric distribution indicates the dominant dimensions affecting

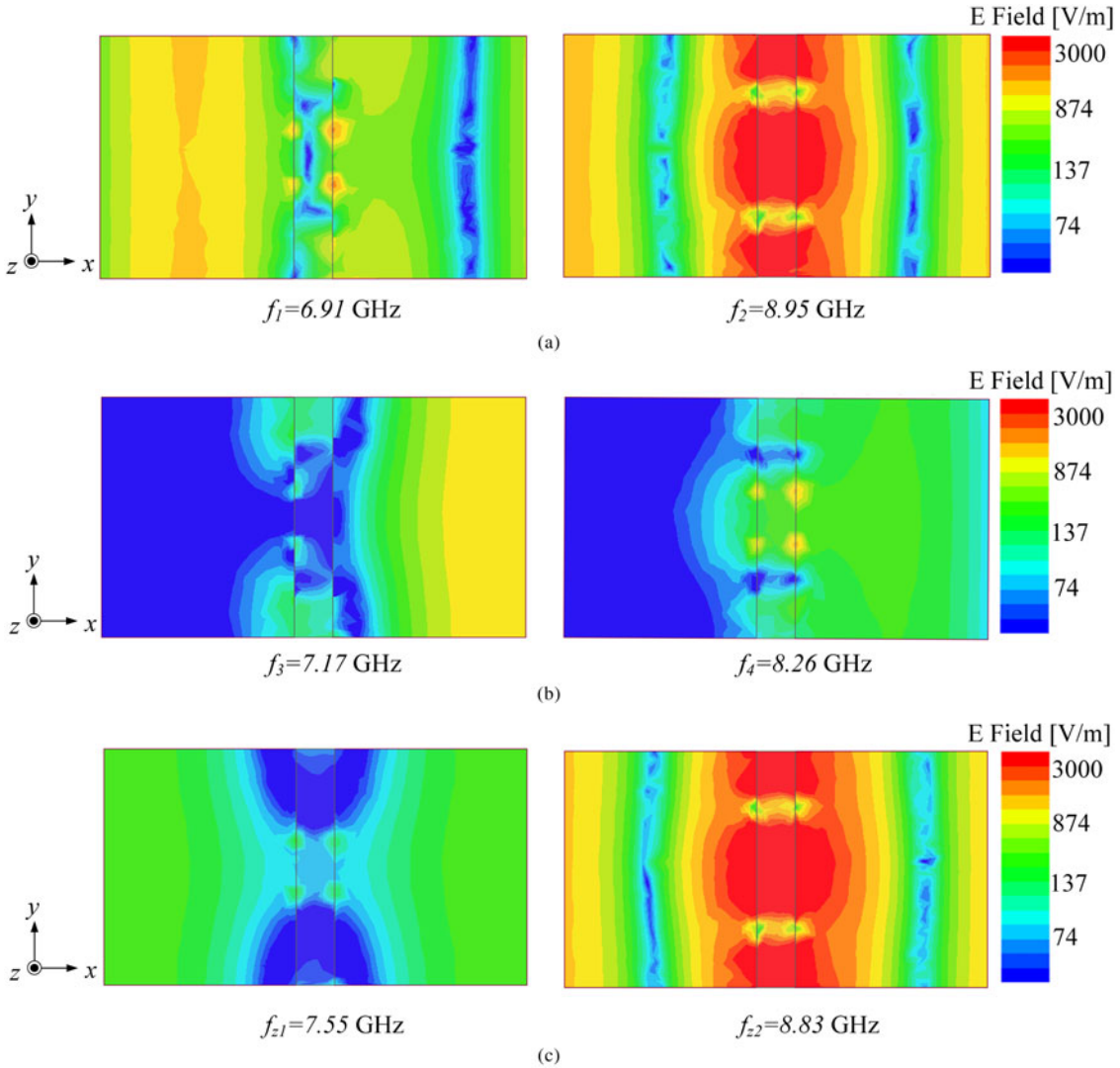

Fig. 3. Electric field distribution in the *xoy*-plane at reflection resonances and zero-refractive-index frequencies inside the waveguide shown in Fig. 1(b) with excitation assigned on port 2. (a) Reflection zeros $f_1 = 6.91$ GHz and $f_2 = 8.95$ GHz, (b) reflection poles $f_3 = 7.17$ GHz and $f_4 = 8.26$ GHz, and (c) zero-refractive-index frequency points $f_{z1} = 7.55$ GHz (MNZ) and $f_{z2} = 8.83$ GHz (ENZ).

https://doi.org/10.1017/S1759078717000526 Published online by Cambridge University Press

the corresponding resonant frequency. As shown in Fig. 4, an electric concentration on the upper and lower parts in the z-direction can be observed at all the frequency resonances f_1, f_2, f_3, f_4, f_{z1}, and f_{z2}, which means that a general frequency shift can be achieved by adjusting the dimension of the upper and lower parts in the z-direction. What's more, the pole f_2 and zero-refractive-index frequency point f_{z2} are also significantly affected by inner fan-shaped patches as shown in Figs 4(a) and 4(c). It is worth pointing out that the position of the tunneling frequency f_{z2} can be independently tuned by changing the dimensions of the inner fan-shaped patches. According to the effective medium characteristics of the proposed FSS, near-zero permeability at f_{z1} and negative permeability at f_3 indicate a dominant H-field resonant behavior, while near-zero permittivity at f_{z2} and negative permittivity at f_4 indicate a dominant E-field resonant behavior. Therefore, by properly adjusting the parameters of the structure, the proposed CSDRR FSS can exhibit a steep high-selective band-reject filtering response, a satisfactory performance of rapid roll-off, and a much lower profile with only a planar single layer. Moreover, it is much appealing for the independent control on the tunneling frequency since the tunneling condition is met only at one specific frequency.

III. PARAMETRIC STUDY AND DISCUSSION

In order to prove the effectiveness of the proposed analytical model described in Section II, a parametric study of the proposed CSDRR FSS related to the filtering responses is carried out.

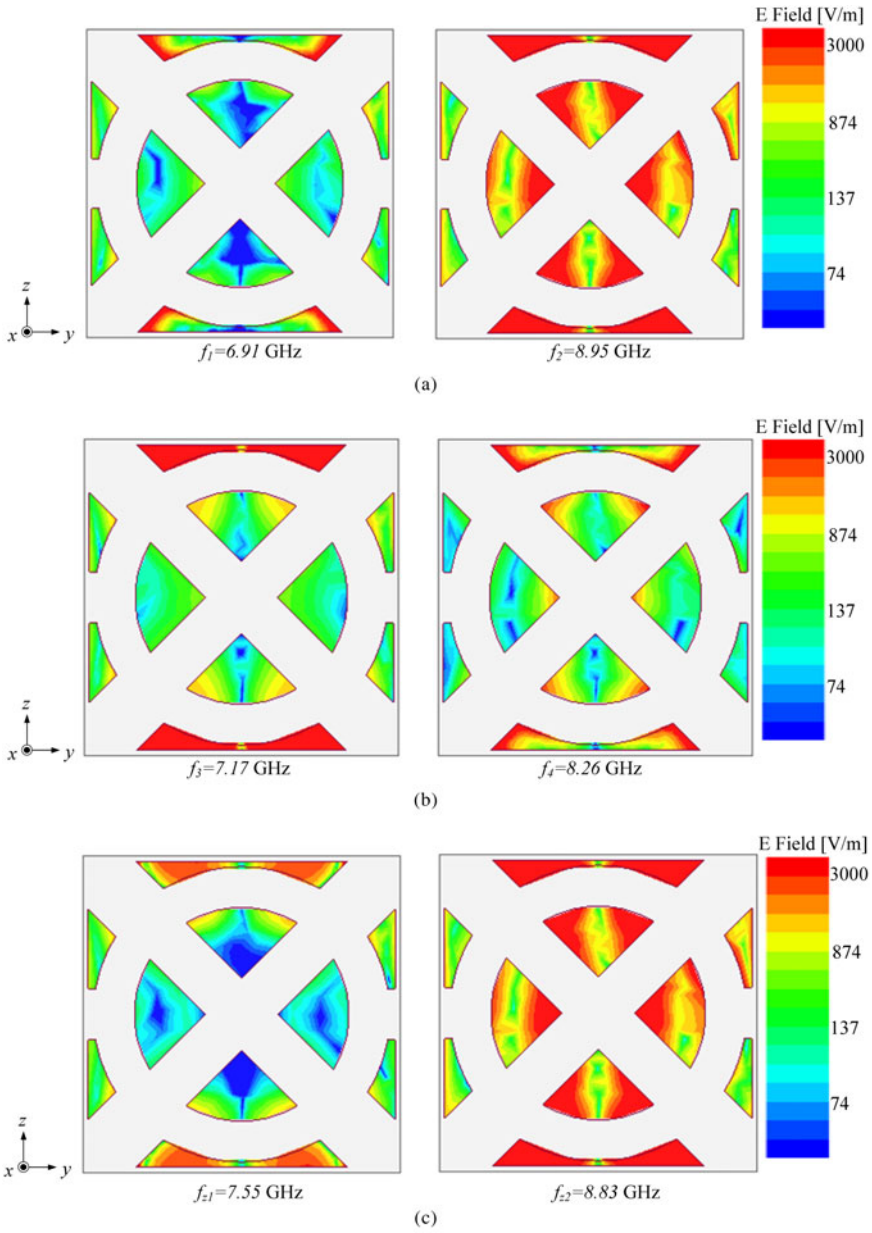

Fig. 4. Electric field distribution of the proposed CSDRR FSS at reflection resonances and zero-refractive-index frequencies. (a) Reflection zeros $f_1 = 6.91$ GHz and $f_2 = 8.95$ GHz, (b) reflection poles $f_3 = 7.17$ GHz and $f_4 = 8.26$ GHz, and (c) zero-refractive-index frequency points $f_{z1} = 7.55$ GHz (MNZ) and $f_{z2} = 8.83$ GHz (ENZ).

https://doi.org/10.1017/S1759078717000526 Published online by Cambridge University Press

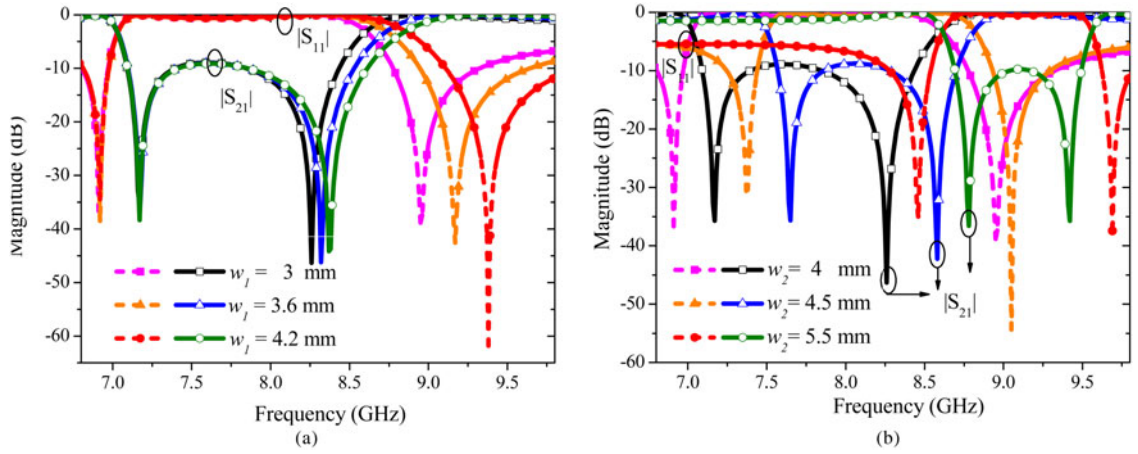

Fig. 5. Filtering responses of the proposed CSDRR FSS changing. (a) Inner width w_1 ($a = 6.3$ mm, $b = 8.7$ mm, $w_2 = 4$ mm, $gap_1 = 0.3$ mm, $gap_2 = 3$ mm, $P = 18$ mm, $h = 3$ mm), and (b) outer width w_2 ($a = 6.3$ mm, $b = 8.7$ mm, $w_1 = 3$ mm, $gap_1 = 0.3$ mm, $gap_2 = 3$ mm, $P = 18$ mm, $h = 3$ mm).

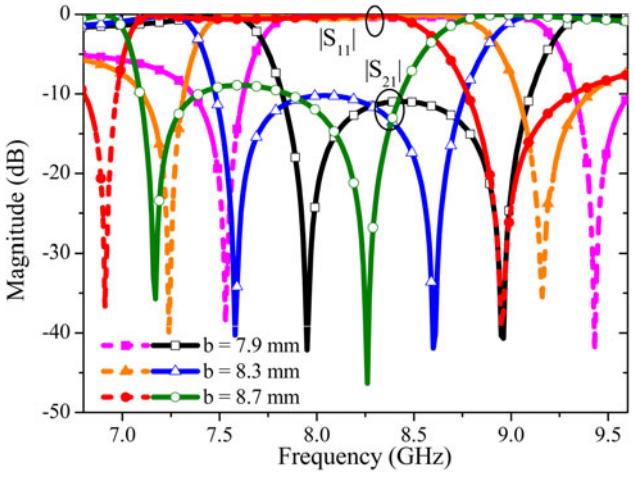

Fig. 6. Filtering responses of the proposed CSDRR FSS with variation in outer annular ring slot b ($a = 6.3$ mm, $w_1 = 3$ mm, $w_2 = 4$ mm, $gap_1 = 0.3$ mm, $gap_2 = 3$ mm, $P = 18$ mm, $h = 3$ mm).

A) Orthogonal slots (w_1, w_2)

The effect of the orthogonal slots width w_1 and w_2 on the filtering responses of the proposed FSS is shown in Fig. 5. According to the analytical model described in Section II, w_1 dominates the adjustment of f_2 and f_{z2} by changing the area of the inner fan-shaped patches. It can then be verified from Fig. 5(a) that while w_1 increases, the tunneling frequency f_{z2} and reflection zero f_2 will shift to higher frequency without influence on other resonant frequencies. It is flexible in the independent adjustment of the tunneling frequency f_{z2}. This phenomenon is due to the fact that the capacitor formed between adjacent electric resonant arms arranged periodically along the y-axis is reduced as w_1 increases, and thus the resonant frequency of electric Lorentz model is increased. The center frequency of the stop-band also shifts to higher frequency accordingly, which leads to a widen stop-band bandwidth and a sharper skirt.

It can be seen from Fig. 5(b) that all resonant points will shift to higher frequency with the increase of w_2. As shown in Fig. 4, increasing w_2 will result in a decrease in the areas of the upper and lower parts in z-direction, which is also the electric field concentration parts. Furthermore, we can see that the reflection zero f_2 presents a much smaller frequency shift compared with the reflection zero f_1 due to the unchanged inner fan-shaped electric field concentration at f_2. Therefore, the center frequency of the stop-band is shifted higher with different frequency shift levels of f_1 and f_2. The bandwidth of stop-band is thus narrowed with the increase of w_2.

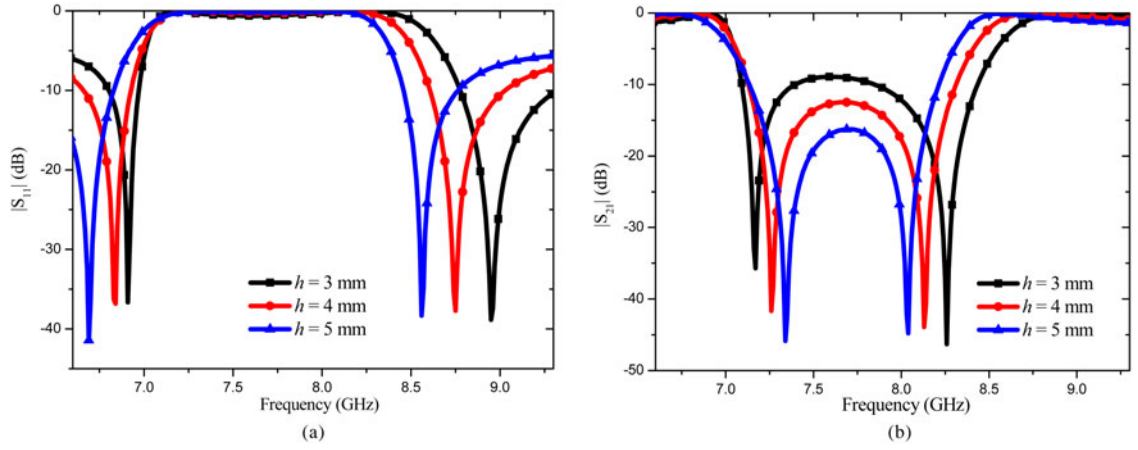

Fig. 7. Frequency responses of the proposed FSS with different h. (a) Reflection coefficient, and (b) transmission coefficient.

https://doi.org/10.1017/S1759078717000526 Published online by Cambridge University Press

Fig. 8. Photograph of the fabricated FSS prototype and measurement system setup, (a) fabricated FSS prototype, and (b) measurement system setup for FSS in the near-field zone.

B) Outer radius of the annular slot (*b*)

As shown in Fig. 1(a), the variation of the outer radius of the annular slot b can be taken as the change of slot length of the proposed FSS. As depicted in Fig. 6, all resonances of the FSS shift to lower frequency with slot length b increase, which is also a well-known fact in the FSS theory. However, it is clearly seen that variation in f_2 is much less significant than in f_1, which is owing to unchanged inner fan-shaped electric field concentration at f_2. As has been discussed in the proposed analytical model, we can correspond different resonant modes to the filtering response at the poles and zeros. As a consequence, the bandwidth of the reject band becomes widen and yet the center frequency shifts to lower band.

C) Substrate thickness (*h*)

It follows from [19] that dielectric loading exerts a significant influence on the filtering response of FSS. We illustrate the effect of the substrate thickness h on the frequency responses of the proposed FSS.

As shown in Fig. 7, resonant frequencies at two reflection zeros f_1 and f_2 decrease with parameter h increase. Moreover, due to the increase of the first reflection pole

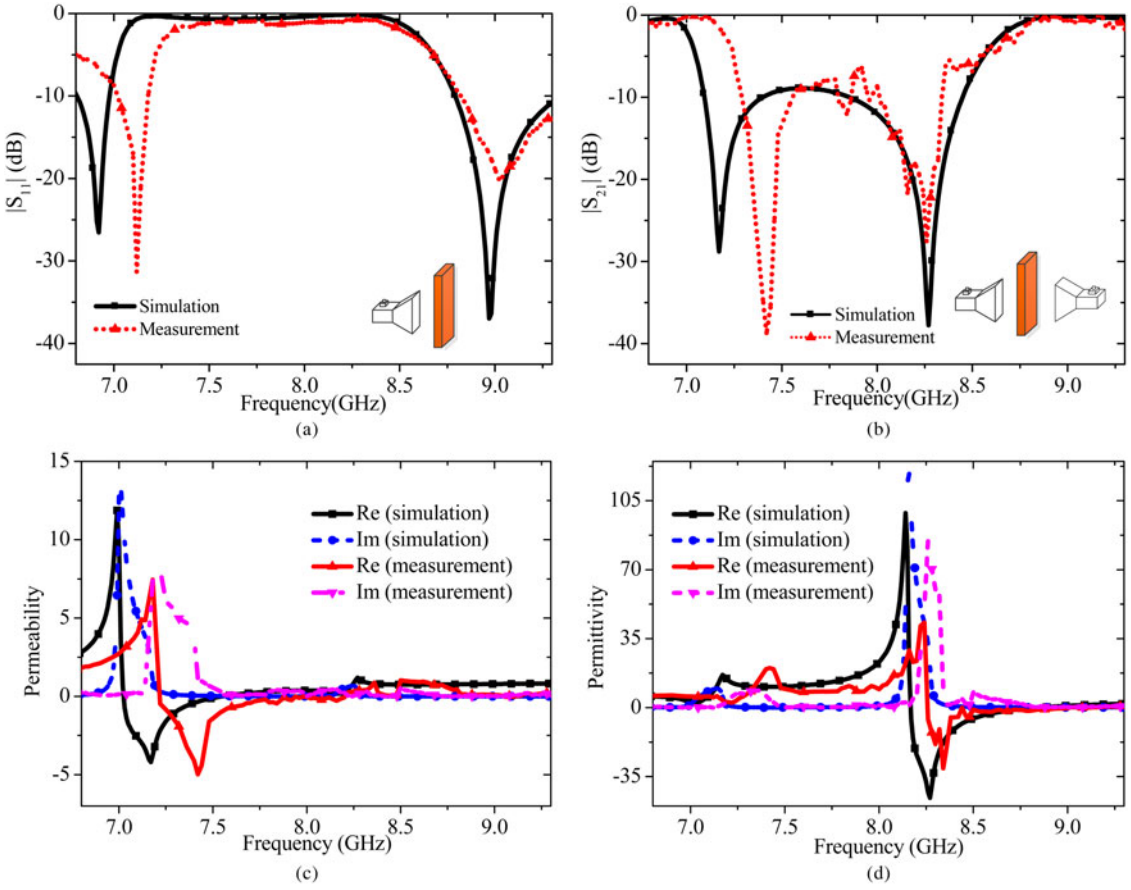

Fig. 9. Comparison of measured and simulated results of the fabricated FSS. (a) S_{11} characteristics from one-port method, (b) S_{21} characteristics from two-port method, where the measurement is preformed after calibration in the near-field region, (c) retrieval effective permeability, and (d) retrieval effective permittivity.

https://doi.org/10.1017/S1759078717000526 Published online by Cambridge University Press

resonance f_3 and the decrease of the second reflection pole resonance f_4, which are depicted in Fig. 7(b), a relatively narrower stop-band bandwidth is obtained.

IV. EXPERIMENTS AND DISCUSSION

Based on aforementioned discussions in Sections II and III, a prototype of the proposed FSS working in the X-band was fabricated and measured to validate the ZIM-based FSS design. As shown in Fig. 8, the measurement system setup consists of two standard gain horns operating in the X-band, acting as the transmitting and receiving antennas, respectively. The Agilent N9918A FieldFox handheld vector network analyzer is utilized here to measure the S parameters of the FSS measurement system. The size of the FSS is 223.2×223.2 mm^2, which is more than the aperture of the standard gain horn to decrease the effect of antenna's diffraction on the FSS performance. The fabricated FSS described above is placed in the middle of the transmitting and receiving antennas. It is worth noting that the center of FSS should be in direct line with that of antenna and the polarizations of the transmitting and receiving antennas are the same.

As shown in Fig. 9, the measured results are compared with the simulated results. It should be noted that the results shown in Fig. 9(b) was measured by using two-port method in the near-field zone. The transmission characteristics of only two horns system without the FSS were measured for calibration. The measured frequency responses after calibration agree well with the simulated ones except for a small frequency shift. In order to decrease the effect of the received horn on the measured performance, one-port measurement method is also implemented, i.e. only the transmitting horn and FSS sample are used in the experiment for S_{11} measurement, as shown in Fig. 9(a). It is worth pointing out that most of the integration of FSS in practical applications is one-port style. Figure 9(c) and 9(d) show the effective permeability and permittivity retrieved from the measured S parameters. The measured and simulated results verify the ZIM-based design concept. However, magnitude fluctuations within and frequency shift of the stop-band are observed when the two-port method is used to test the FSS, which is due to the near-field coupling and interaction between two horn antennas. The slight discrepancies between the measured and simulated results are mainly caused by the manufacturing tolerance as well as the instability of dielectric substrate in the experiment. A measurement of the dimensions of the fabricated FSS is taken to compare with the designed prototype and explain the frequency shift of the measurement. Most of the fabricated dimensions are as accurate as 0.1 mm, while the parameters b and gap_2 are varied by decreasing 0.2 and 0.2 mm, respectively. Judging from Section III.B, the filtering response shifts to higher frequency with decrease in b, which explains the frequency shift of the measurement. On the other hand, the variation of gap_2 slightly influences the frequency selective performance of the FSS, which can explain the slight discrepancies of the magnitudes between the measured and simulated results.

V. CONCLUSION

A new type of band-reject FSS based on dual-band ZIM is proposed in this paper. A planar single layer of CDSRR element is designed to provide near-zero effective permeability and effective permittivity in two frequency bands, respectively. Then a new ZIM-based design concept is adopted to make a thorough analysis of the proposed FSS filtering response. The ENZ tunneling frequency can be independently adjusted for specific filtering requirement. The measurement results are in good agreement with simulation results. The ZIM-based design technique gives a new insight into the FSS design and applications.

ACKNOWLEDGEMENTS

This work is supported by the National Natural Science Foundation of China under Contract No. 51477126 and 61501341, and Technology Innovation Research Project of the CETC, AreoSpace T.T.&C. Innovation Program (2015B12), and Fundamental research funds for the Central Universities (JB150205).

REFERENCES

[1] Munk, B.A.: Frequency Selective Surfaces Theory and Design, John Wiley & Sons Press, New York, 2000, 1st edn.

[2] Werner, D.H.; Ganguly, S.: An overview of fractal antenna engineering research. IEEE Antennas Propag., **45** (2003), 38–57.

[3] Wu, T.K. (ed.): Frequency Selective Surface and Grid Array, Wiley-Interscience, New York, 1995, 1st edn.

[4] Yan, M. et al.: A tri-band, highly selective, bandpass FSS using cascaded multilayer loop arrays. IEEE Trans. Antennas Propag., **64** (2016), 2046–2049.

[5] Zhang, T.; Ouslimani, H.H.; Letestu, Y.; Le Bayon, A.; Darvil, L.R.: A low profile multilayer seventh order band-pass frequency selective surface (FSS) for millimeter-wave application, in Proc. IEEE 13th Annu. Wireless and Microwave Technology Conf., April 2012, 1–4.

[6] Omar, A.A.; Shen, Z.: Multiband high-order bandstop 3-D frequency-selective structures. IEEE Trans. Antennas Propag., **64** (2016), 2217–2226.

[7] Zhu, X.C. et al.: Design of a bandwidth-enhanced polarization rotating frequency selective surface. IEEE Trans. Antennas Propag., **62** (2014), 940–944.

[8] Zhou, H.; Hong, W.; Tian, L.; Jiang, M.: A polarization-rotating SIW reflective surface with two sharp band edges. IEEE Antennas Wireless Propag. Lett., **15** (2016), 130–134.

[9] Rashid, A.K.; Shen, Z.: A novel band-reject frequency selective surface with pseudo-elliptic response. IEEE Trans. Antennas Propag., **58** (2010), 1220–1226.

[10] Rashid, A.K.; Shen, Z.: Bandpass frequency selective surface based on a two-dimensional periodic array of shielded of microstrip lines, in Proc. IEEE Antennas Propag. Symp., July, 2010, 1–4.

[11] Enoch, S.; Tayeb, G.; Sabouroux, P.; Guérin, N.; Vincent, P.: A metamaterial for directive emission. Phys. Rev. Lett., **89** (2002), 213902.

[12] Ziolkowski, R.W.: Propagation in and scattering from a matched metamaterial having a zero index of refraction. Phys. Rev. E, **70** (2004), 046608-1–046608-12.

[13] Li, D.Y.; Szabó, Z.; Qing, X.M.; Li, E.P.; Chen, Z.N.: A high gain antenna with an optimized metamaterial inspired superstrate. IEEE Trans. Antennas Propag., **60** (2012), 6018–6023.

https://doi.org/10.1017/S1759078717000526 Published online by Cambridge University Press

[14] Ju, J., Kim, D.; Lee, W.J.; Choi, J.I.: Wideband high-gain antenna using metamaterial superstrate with the zero refractive index. Microw. Opt. Technol. Lett., **51** (2009), 1973–1976.

[15] Silveirinha, M.; Engheta, N.: Tunneling of electromagnetic energy through subwavelength channels and bends using ϵ-near-zero materials. Phys. Rev. Lett., **97** (2006), 157403.

[16] Vojnovic, N.; Jokanovic, B.; Radovanovic, M.; Medina, F.; Mesa, F.: Modeling of nonresonant longitudinal and inclined slots for resonance tuning in ENZ waveguide structures. IEEE Trans. Antennas Propag., **63** (2015), 5107–5113.

[17] Smith, D.R.; Pendry, J.B.: Homogenization of metamaterials by field averaging. J. Opt. Soc. Am. B, **23** (2006), 391–403.

[18] Szabó, Z.; Park, G.H.; Hedge, R.; Li, E.P.: A unique extraction of metamaterial parameters based on Kramers–Kronig relationship. IEEE Trans. Microw. Theory Tech., **58** (2010), 2646–2653.

[19] Luebbers, R.J.; Munk, B.A.: Some effects of dielectric loading on periodic slot arrays. IEEE Trans. Antennas Propag., **26** (1978), 536–542.

[20] Schurig, D.; Mock, J.J.; Smith, D.R.: Electric-field-coupled resonators for negative permittivity metamaterials. Appl. Phys. Lett., **88** (2006), 041109.

[21] Katsarakis, N.; Koschny, T.; Kafesaki, M.; Economou, E.N.; Soukoulis, C.M.: Electric coupling to the magnetic resonance of split ring resonators. Appl. Phys. Lett., **84** (2004), 2943–2945.

[22] Kong, J.A.: Electromagnetic Wave Theory, John Wiley & Sons, New York, 1990, 2st edn.

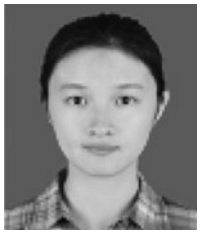

Rui Xi was born in Shandong Province, China, in 1990. She received the B.E. degree in Electronic and Information Engineering from Shandong Normal University, Jinan, China, in 2012. She is currently pursuing the Ph.D. degree in Electromagnetic Fields and Microwave Technology from the National Laboratory of Science and Technology on Antennas and Microwaves, Xidian University, Xi'an, China. Her research interests include frequency-selective surface and high-gain metamaterial antenna.

Long Li (M'06–SM'11) was born in Guizhou Province, China. He received the B.E. and Ph.D. degrees in Electromagnetic Fields and Microwave Technology from Xidian University, Xi'an, China, in 1998 and 2005, respectively. He was a Senior Research Associate in the Wireless Communications Research Center, City University of Hong Kong in 2006. He received the Japan Society for Promotion of Science (JSPS) Postdoctoral Fellowship and visited Tohoku University, Sendai, Japan, as a JSPS Fellow from November 2006 to November 2008. He was a Senior Visiting Scholar in the Pennsylvania State University, USA, from December 2013 to July 2014. He is currently a Professor in the School of Electronic Engineering, Xidian University. His research interests include metamaterials, computational electromagnetics, electromagnetic compatibility, novel antennas and microwave devices design, and Orbital Angular Momentum. Dr. Li received the Nomination Award of National Excellent Doctoral Dissertation of China in 2007. He won the Best Paper Award in the International Symposium on Antennas and Propagation in 2008. He received the Program for New Century Excellent Talents in University of the Ministry of Education of China in 2010. Dr. Li is a senior member of the Chinese Institute of Electronics (CIE).

Yan Shi received the B.Eng. and Ph.D. degrees in Electromagnetic Fields and Microwave Technology from Xidian University, Xi'an, China, in 2001 and 2005, respectively. He joined the School of Electronic Engineering, Xidian University, in 2005 and was promoted to full Professor in 2011. From 2007 to 2008, he worked at City University of Hong Kong, Hong Kong, China, as a Senior Research Associate. From 2009 to 2010, he was a Visiting Postdoctoral Research Associate with the University of Illinois at Urbana-Champaign. He has authors or coauthored over 100 papers in referred journal and a book (Notes on catastrophe theory, Beijing: Science Press, 2015). His research interests cover computational electromagnetics, metamaterial, antenna, and electromagnetic compatibility. Dr. Shi is senior members of and IEEE and Chinese Institute of Electronics (CIE).

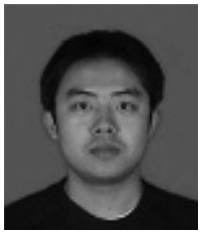

Cheng Zhu, Ph.D., received the Bachelor degree in Electronic Engineering from Xidian University, Xi'an, Shaanxi, China, in 2006. Since 2007, he has taken a combined master–doctor program and worked for Ph.D. in Xidian University. He received his Ph.D. degree in 2011 and then became a teaching-research faculty. Now he is an associate professor and a member of the Key Laboratory of Science and Technology on Antennas and Microwaves. His current research interests involve Metamaterials, Antenna Theory and Design, and Orbital Angular Momentum. Dr. Zhu is the recipient of the honorable mention at the IEEE AP-S Student Contest Award from 2010 IEEE AP-S/URSI Symposium, Toronto, Canada.

Xi Chen was born in Xi'an, China, in June 1982. She received the B.Eng. degree in Electronic Engineering and the Ph.D. degree in Electromagnetic Fields and Microwave Technology from Xidian University, Xi'an, China, in 2005 and 2011, respectively. She is currently a lecturer in the School of Electronic Engineering, Xidian University. She has been engaged in the development of metamaterials. Her current research interests involve both characteristics of electromagnetic bandgap structure (EBG) and its applications. Dr. Chen currently works in Xidian University as a lecturer. She has been engaged in the development of metamaterials. Her current research interests involve EBG and its applications.

https://doi.org/10.1017/S1759078717000526 Published online by Cambridge University Press